Research Article | Vol. 13, No. 9 / 1 Sep 2022 / Biomedical Optics Express 4510
Biomedical Optics EXPRESS

Multiple forward scattering reduces the measured scattering coefficient of whole blood in visible-light optical coherence tomography

RAYMOND FANG,[1,2] IAN RUBINOFF,[1,2,*] AND HAO F. ZHANG[1]

[1]Department of Biomedical Engineering, Northwestern University, Evanston IL 60208, USA
[2]These authors contributed equally to this work
[*]IanRubinoff2022@u.northwestern.edu

Abstract: The optical properties of blood encode oxygen-dependent information. Noninvasive optical detection of these properties is increasingly desirable to extract biomarkers for tissue health. Recently, visible-light optical coherence tomography (vis-OCT) demonstrated retinal oxygen saturation (sO_2) measurements by inversely measuring the oxygen-dependent absorption and scattering coefficients of whole blood. However, vis-OCT may be sensitive to optical scattering properties of whole blood, different from those reported in the literature. Incorrect assumptions of such properties can add additional uncertainties or biases to vis-OCT's sO_2 model. This work investigates whole blood's scattering coefficient measured by vis-OCT. Using Monte Carlo simulation of a retinal vessel, we determined that vis-OCT almost exclusively detects multiple-scattered photons in whole blood. Meanwhile, photons mostly forward scatter in whole blood within the visible spectral range, allowing photons to maintain ballistic paths and penetrate deeply, leading to a reduction in the measured scattering coefficient. We defined a scattering scaling factor (SSF) to account for such a reduction and found that SSF varied with measurement conditions, such as numerical aperture, depth resolution, and depth selection. We further experimentally validated SSF in *ex vivo* blood phantoms with pre-set sO_2 levels and in the human retina, both of which agreed well with our simulation.

1. Introduction

Optical coherence tomography (OCT) enabled noninvasive three-dimensional (3D) retinal imaging at micrometer-scale volumetric resolutions [1,2]. Since its first report 30 years ago, OCT has become the clinical gold standard for diagnosing and monitoring nearly all major ocular diseases [3,4].

OCT's sensitivity to optical scattering and absorption provides imaging contrast between tissues and may be used to probe tissue health [5–8]. These capabilities extend to whole blood (further referred to as blood), where absorption and scattering are wavelength-dependent and oxygen-dependent [9–12]. Applying short-time Fourier transforms (STFTs), OCT can measure wavelength-dependent attenuations of blood with micrometer-scale depth resolution, enabling the measurement of oxygen saturation (sO_2) in discrete blood vessels [13–17]. Studies suggested that alterations in retinal sO_2 can be a sensitive biomarker for blindness-causing diseases, including glaucoma and diabetic retinopathy [18,19]. Hence, accurate and noninvasive retinal sO_2 measurement can improve the clinical management of these diseases.

Blood's optical absorption properties are 2-3 orders of magnitude higher in the visible spectral range than the near-infrared (NIR) spectral range [12], enabling recently developed visible-light OCT (vis-OCT) [14] to overcome the fundamental optical contrast limit in NIR OCTs [16,20]. In 2013, Yi et al. showed that vis-OCT is sensitive to retinal sO_2 in rodents. Later on, vis-OCT retinal oximetry was demonstrated in rodents [21–24] and humans [25,26].

#459607 https://doi.org/10.1364/BOE.459607
Journal © 2022 Received 28 Mar 2022; revised 18 Jul 2022; accepted 19 Jul 2022; published 2 Aug 2022

Biomedical Optics EXPRESS

Vis-OCT relies on the reported optical properties of whole blood to estimate sO_2. In the visible spectral range, Mie theory predicts an average absorption coefficient (μ_a) near 150 cm^{-1} and an average scattering coefficient (μ_s) near 3000 cm^{-1} [12,27]. However, a wide range of experimentally measured values have been reported, suggesting uncertainty in the measured optical properties of blood, and potentially reducing the reliability of vis-OCT oximetry [9–11,27–29]. For example, some measured μ_s values are ~ 1/3 of the Mie theory prediction [9,28,30]. Researchers attributed such a reduction in μ_s to the blood's 'packing factor', which describes correlated optical interactions between densely packed RBCs and their hematocrit-dependence [9,28]. Our group previously used the packing factor (denoted as W) to scale μ_s in the vis-OCT inverse fitting model for sO_2 measurement [30]. Specifically, our group found that the model's goodness of fit (R^2) maximized when W was between 0.2 and 0.4. This W value was consistent with the definition of the packing factor, which scales μ_s by ~ 1/3 at physiological hematocrit [9]. Several other vis-OCT retinal oximetry works also used this W range to scale μ_s [21,25,30,31].

However, reported vis-OCT oximetry methods accounted for blood's μ_s differently, among which significant discrepancies exist [7,22,23,30,32–35]. Since vis-OCT oximetry fits the measured spectrum to the literature-reported μ_a and μ_s, deviations between the measured and reported μ_s can introduce sO_2 measurement error. Therefore, accurate and consistent quantification of sO_2 benefits from a systemic investigation on how vis-OCT measures μ_s. We systemically investigated measuring optical scattering properties of blood detected by vis-OCT. First, we performed Monte Carlo (MC) simulations of a retinal blood vessel and photon detection by vis-OCT.

MC simulation provides a statistical approximation of complex light-tissue interactions that are not trivial to be modeled mathematically. Furthermore, MC simulation is not susceptible to systemic biases present in practical OCT detection or image reconstruction [35–37] and, therefore, is useful for modeling OCT images of tissue. For each photon packet exiting the tissue, we monitored the number of scattering events and optical pathlength traveled in tissue to investigate the impact of multiple scattering on the vis-OCT signal. We reconstructed simulated vis-OCT A-lines to establish a direct relationship between multiple scattering and the measured μ_s. Then we established the scattering scaling factor (SSF), a generalized scaling coefficient for μ_s. Since multiple scattering influenced the measured μ_s, we further investigated photon detection by different numerical apertures (NAs), because NA acts as a geometric filter in detecting multiply scattered photons. Second, we compared our simulation results to experimental vis-OCT imaging of *ex vivo* blood phantoms. We found excellent agreement between the simulated and experimentally measured values across pre-set oxygenation levels. Finally, we validated our SSF analysis in human retina vis-OCT imaging and found a strong agreement with our simulated results. Validated by simulation, *ex vivo* blood phantom imaging, and *in vivo* human retinal imaging, we provide evidence that vis-OCT measured μ_s is smaller than the reported packing factor but higher than the reduced scattering coefficient (μ_s') [35,38]. This work sets the foundation for a unified theory of vis-OCT-measured optical properties of blood and more robust retinal oximetry.

1.1. Detecting scattered light with OCT

Most OCT's use NIR (800 nm – 1300 nm) illumination, where biological tissues have lower optical scattering coefficients ($\mu_s < 100\ cm^{-1}$), lower optical absorption coefficients ($\mu_a < 1\ cm^{-1}$), and moderately high scattering anisotropy ($0.7 < g < 0.9$) [39]. Such optical properties yield mean-free-paths (MFPs) of several hundred micrometers in tissue, meaning photons can travel deep into tissues before being multiply scattered. Since OCT's axial resolution is dominated by light's coherence length and not geometrical optics, OCT can use a low NA to image deeply penetrating photons across several hundred micrometers with axial resolutions < 10 µm [40].

Biomedical Optics EXPRESS

Another benefit of imaging weakly scattering tissues with a low NA is high sensitivity to single-scattered or ballistic photons [41]. In this work, we define ballistic photons as Class I photons [35], which satisfy

$$|2z_{max} - D| \leq \frac{l_c}{2}, \tag{1}$$

where z_{max} [μm] is the maximum depth a photon travels in the tissue with respect to the OCT's zero delay; D [μm] is the total optical path traveled by the photons with respect to the OCT's zero delay; and l_c [μm] is the coherence length. Essentially, a Class I photon travels straight, allowing only a slight deviation within l_c. We define Class II photons as photons that do not travel in a straight line before being detected by the OCT, which satisfy

$$|2z_{max} - D| > \frac{l_c}{2}. \tag{2}$$

Finally, we define those photons undetectable by the OCT system as Class III photons.

Figs. 1(A) & 1B illustrate OCT imaging in a weakly scattering tissue (e.g. $\mu_s < 100\,\mathrm{cm}^{-1}$ and $0.7 < g < 0.9$) using a low NA (e.g. < 0.2). Fig. 1(A) shows a global illustration of tissue with optical properties within the NIR spectral range. The OCT sample arm focuses light on a spot in the tissue (illustrated by the green oval), which creates an A-line at that location. Due to the low NA, incident photons (green arrow) are nearly perpendicular to the tissue surface. Since the focus spot creates a conjugate point with the sample arm detector, it also acts as a geometric projection of the detector itself [42]. Only photons collected within the spot and the solid angle defined by the illumination NA will contribute to the A-line.

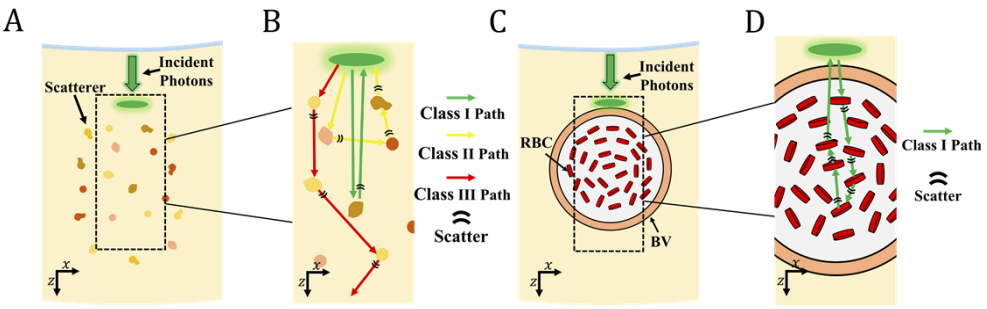

Fig. 1. (A) Illustration of OCT illumination of a weakly scattering medium. Incident photons (green arrow) create a focal spot (green oval) and detection aperture in the tissue; (B) Magnified illustration of the highlighted region in panel A, showing the paths of Class I (green arrow), Class II (yellow arrow), and Class III photons (red arrow); (C) Illustration of vis-OCT illumination of a retinal blood vessel (RBC) containing red blood cells (RBC); (D) Magnified illustration of the highlighted region in panel C, showing the paths of Class I photons (green arrow).

Fig. 1(B) is a magnified illustration of Fig. 1(A) in the black-dashed box. The green, yellow, and red arrows respectively illustrate representative paths of Class I, Class II, and Class III photons. The black bands represent scattering events. The Class I photon travels deeply into the tissue, scatters once, reverses direction, and returns along almost the same path in the z-direction (also referred to as backscattering). The Class II photons are scattered multiple times and travel significantly along the x-direction before returning to the detector. The Class III photons are scattered multiple times deeply in the tissue and do not return to the detector. Under the conditions of $\mu_s < 100\,\mathrm{cm}^{-1}$ and $0.7 < g < 0.9$, photons can travel tens or hundreds of μm along the x-direction after each scattering event. Therefore, multiply scattered photons are increasingly likely to be Class III rather than Class II photons since they will travel too far from the detector

Biomedical Optics EXPRESS

before being absorbed by tissue or escaping the tissue. Meanwhile, most detected photons are likely to be Class I photons (green arrow in Fig. 1(B) since they do not have the opportunity to travel outside the detection region.

When most photons are Class I and single scattered, the OCT A-line can be modeled by the Beer-Lambert Law [43]

$$A(z)^2 \propto e^{-2(\mu_a+\mu_s)z}, \tag{3}$$

where $A(z)^2$ [arbitrary unit] is the A-line intensity; z [mm] is the depth in the tissue; and the coefficient 2 in the exponential term indicates round trip in tissue. Eq. 3 has been thoroughly derived and experimentally validated for Class I photons [6]. Vis-OCT imaging of blood represents a special scenario that deviates from the assumptions described in Figs. 1(A) & 1B. The reported μ_s for oxygenated and deoxygenated blood states are $> 3000\,\mathrm{cm}^{-1}$ and the W-scaled μ_s are near $1000\,\mathrm{cm}^{-1}$ [9]. Both these μ_s values are over an order of magnitude greater than μ_s values ($< 100\,\mathrm{cm}^{-1}$) typical of most tissues within NIR spectral range. Furthermore, blood is more highly forward scattering ($g \geq 0.98$) than most tissues ($0.7 < g < 0.9$). Assuming normal incidence of light on a vessel (Fig. 1(C), photons can be multiply scattered and still satisfy the Class I condition. Fig. 1(D) illustrates such a path following the green arrow. We hypothesize that the path shown in Fig. 1(D) is a common, if not dominant, detection scenario in blood imaging using vis-OCT. A Class I photon that travels deeper than its single scatter assumption is equivalent to reducing its μ_s in Eq. 3. Previously, Thrane et al. developed a model for OCT incorporating multiple scattering using the extended Huygens-Fresnel [44] principle, which Almasian et al. verified in silica beads with μ_s up to $97\,\mathrm{cm}^{-1}$ and g up to 0.9. Their theoretical model predicted a reduction in the OCT measured μ_s, which is dependent on g, numerical aperture, and location of the tissue relative to the focal plane [5]. Here, we account for the reduction in μ_s by rewriting the Beer-Lambert Law as

$$A(z)^2 \propto e^{-2(\mu_a+SSF\mu_s)z} \tag{4}$$

where SSF [dimensionless] is the scattering scaling factor, which is < 1 and scales μ_s to account for the increased detection of photons deeper in tissue. The SSF is a generalized scaling factor and incorporates any other reductions of μ_s, including W.

1.2. Vis-OCT oximetry

Oxygenated and deoxygenated blood have distinct wavelength-dependent μ_a and μ_s, allowing estimation of sO_2. An STFT [45] can reconstruct spectrally-dependent A-lines, which can be modeled by

$$\begin{aligned}\log(A(\lambda,z)^2) \propto\ & -2[\mathrm{sO_2}\mu_{\mathrm{aHbO_2}}(\lambda) + (1-\mathrm{sO_2})\mu_{\mathrm{aHb}}(\lambda) + \mathrm{SSF}\times \mathrm{sO_2}\mu_{\mathrm{sHbO_2}}(\lambda) + \\ & SSF\times(1-\mathrm{sO_2})\mu_{\mathrm{sHb}}(\lambda)]z,\end{aligned} \tag{5}$$

where λ [nm] is the central wavelength of the selected STFT sub-band; sO_2 [dimensionless, between 0 and 1] is the oxygen saturation in blood; the subscripts HbO_2 and Hb denote oxygenated or deoxygenated hemoglobin, respectively; and SSF [dimensionless] is the scattering scaling factor. We used 21 STFT sub-bands ranging from 528 nm to 588 nm equidistant in wavenumber, with an average full-width-at-half-max (FWHM) bandwidth of 11 nm.

2. Methods

2.1. MC simulation parameters

We simulated vis-OCT detection and reconstruction in a retinal blood vessel using MC simulation [8,27,35,38,46–50]. Fig. 2(A) shows the beam incident on the cornea, after which light is focused

Biomedical Optics EXPRESS

onto the retina. Fig. 2(B) shows a cross-sectional view of the multi-layered 3D model of a blood vessel embedded in the retina. We modeled the blood vessel using an infinitely long cylinder located 55 µm below the vitreous-retina interface. The vessel has three concentric layers: blood, cell-free zone (CFZ) [33,34], and the vessel wall. The CFZ is a thin layer consisting primarily of plasma between the blood and the vessel wall. It arises from the difference in viscosity between RBCs and plasma and is described by the Fahraeus Lindqvist (FL) effect [51]. The CFZ has been previously observed in OCT images [52] and is noticeable in our vis-OCT data. Table 1 summarizes the optical and geometrical parameters. We extracted the properties of the retina [27,48], vessel wall [27], and CFZ [53] from the literature. We used the theoretical optical properties of blood previously derived by Faber et al. [12,27]. To increase the speed of our simulation, we used the average μ_a and μ_s between 520 nm and 600 nm (center wavelength 560 nm). Although there is still uncertainty in the exact values of μ_a, μ_s, and g [9], our values are well within the reported range [9–11,27–29]. To account for correlated optical interactions between densely packed RBCs, we scaled blood's μ_s using the packing factor $W = (1 - H)^2$, where H is hematocrit [dimensionless]. Assuming a hematocrit of 45% [54], we have $W = 0.3025$.

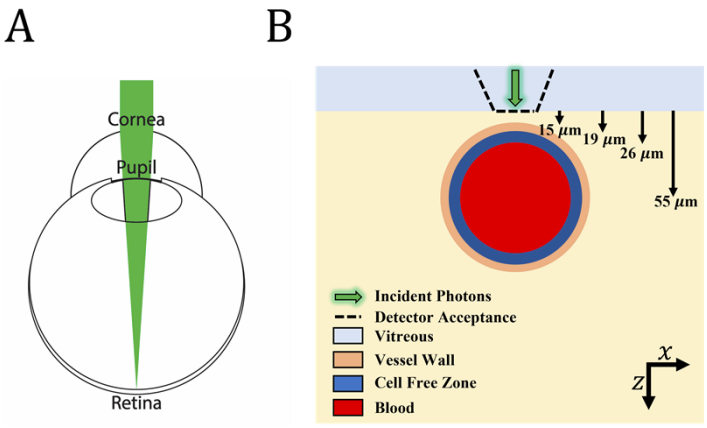

Fig. 2. (A) Illustration of the beam incident on the cornea. (B) Illustration of tissue and imaging geometry in Monte Carlo simulation. Downward arrows (from left to right) highlight the interface depths of the vessel wall, cell-free zone, and blood, respectively; the fourth arrow highlights the depth of the vessel center.

2.2. MC simulation algorithm

MC simulation of photon propagation in biological tissue has been widely reported [8,27,35,38,46–50,55]. We followed the algorithm of simulating photon transport in multi-layered tissues (MCML) in 3D [38]. Briefly, we launch an infinitely narrow photon beam towards the retina and blood vessel, as illustrated in Fig 2. Each photon packet's launching position is at the vitreous-retina interface (Fig. 2(B) at the lateral center of the vessel. The initial direction vector is along the z-axis. Upon tissue entry, we generated the step size (s) following the Poisson distribution

$$s = \frac{-\ln(\xi)}{\mu_t}, \tag{6}$$

where $\mu_t = \mu_a + \mu_s$ and ξ [dimensionless] is a random variable following a uniform distribution between 0 and 1. After traveling a distance s, the photon packet interacts with tissue and deposits a fraction $\frac{\mu_a}{\mu_t}$ of its weight. At each interaction location, the photon packet is scattered by an angle θ relative to its current propagation direction determined by the Henyey-Greenstein phase

Biomedical Optics EXPRESS

function [55]

$$p(\theta) = \frac{1}{4\pi} * \frac{1-g^2}{(1+g^2-2gcos(\theta))^{\frac{3}{2}}}. \quad (7)$$

At the interface between two media, the photon packet either reflects or transmits with probabilities according to Fresnel's equations [56]. Upon entering a new tissue region, μ_t is adjusted accordingly. The simulation continues until the photon packet exits the retina into the vitreous or the optical path distance traveled is greater than 2000 μm, well beyond the depth of the blood vessel.

If the photon packet exits the retina into the vitreous, we recorded the remaining weight of the photon packet, the optical pathlength traveled within the tissue, the total number of scattering events in all tissue regions, the total number of scattering events in blood, the exiting position, and the exit angle. We simulated 10^{10} photon packets for each A-line. We implemented the simulation in MATLAB 2020 using parallel computing on a PC with a 3.4-GHz Intel Core i7-6800 K CPU and 64-GB RAM. The simulation of an A-line took approximately 120 hours to complete.

2.3. Photon detection

To simulate OCT detection, we geometrically filtered photons exiting the retina [50] (black-dashed lines in Fig. 2(B). We determined photon acceptance aperture and angle according to the NA of the light incident on the retina. We tested the NA value from 0.015 to 0.112, which follows the optical properties of normal human eyes [57]. We calculated the NA as

$$NA = n \cdot \sin\left(tan^{-1}\frac{D}{2f}\right), \quad (8)$$

where n [dimensionless] 1.35 is the refractive index; D [cm] is the $1/e^2$ diameter of the collimated beam incident on the cornea; f [cm] 1.8 cm is the focal length of a normal eye [58]; and $\tan^{-1}\frac{D}{2f}$ is the acceptance angle with respect to normal incidence. We used the NA to calculate the focal spot beam waist

$$w = n\frac{2\lambda}{\pi NA}, \quad (9)$$

where $\lambda = 560$ nm is the central wavelength of the vis-OCT probing light. For simplicity, we detect photons using a uniform circle with a radius of w. In the results, we use an NA = 0.05, equivalent to a 2.9° acceptance angle and a detection diameter of $2w$ = 7.0 μm unless otherwise specified.

2.4. Vis-OCT A-line reconstruction

We reconstructed simulated vis-OCT A-lines using the recorded photon weights and optical path distances in the simulation. We only used photons detected under the acceptance conditions. Adopting the methods in Kirillin et al. [50], we reconstructed the OCT A-line as

$$A(z)^2 = \sum_{i=1}^{N_{photons}} W_i \exp\left(-\left(\frac{2z-D_i}{l_c}\right)^2\right), \quad (10)$$

where W_i [dimensionless] is the photon weight; D_i [cm] is the optical path distance; and l_c [μm] is the axial resolution. We note that our Monte Carlo simulation does not interfere sample arm and reference arm electric fields as in a real OCT system, which measures the square root of the A-line intensity [40,59]. Therefore, the simulated A-line is assumed to be directly proportional to A-line intensity $A^2(z)$ and does not need to be squared. We set the distance between adjacent z positions as 1 μm and used an axial resolution of 9 μm defined by the l_c of the STFT sub-band window centered at 558 nm with an FWHM bandwidth of 11 nm [40]. We used this sub-band window size for spectroscopic A-line reconstruction in our experimental studies.

Biomedical Optics EXPRESS

2.5. Experimental measurements of ex vivo blood samples

We used the vis-OCT system operating from 510 to 610 nm described by Beckmann et al. [60] to image *ex vivo* blood samples in phantom vessels. The imaging objective in the sample arm had an NA of 0.05 [61], consistent with our simulation and human imaging. Briefly, we constructed a vessel phantom by pulling a glass capillary tube to have an inner diameter of 200 μm and embedded and stabilized the tube in a plastic well. To reduce the influence of specular reflections, we added immersion oil to the well until the tube was covered. We prepared whole bovine blood (Quadfive, Ryegate, MT) of hematocrit 45% of oxygen levels ranging from 45% to > 99%. To oxygenate the blood, we added a constant stream of pure oxygen and stirred the blood with a magnetic stir bar. To deoxygenate the blood, we added sodium dithionite [62] to the solution and stirred. We repeated these processes until reaching the desired oxygen level. We monitored blood's partial pressure of oxygen (pO_2), partial pressure of carbon dioxide (pCO_2), pH, and temperature using a blood-gas analyzer (Rapidlab 248, Siemens Healthcare Diagnostics, Malvern, PA) and estimated the corresponding sO_2 [63]. Before loading the tube with blood, we flushed it with a phosphate-buffered saline and heparin solution to reduce clotting or sedimentation. Finally, we loaded the tube with blood and flowed it at 0.3 mm/s using a syringe pump (Fusion 100, Chemyx, Inc. Stafford, TX). We aligned the tube to be in focus and near the system zero-delay and illuminated it with 1.20 mW of power. Finally, we acquired data consisting of 512 A-lines × 256 B-scans with imaging range 1 mm × 1 mm at a 25 kHz A-line rate.

2.6. Experimental measurement of human retinal vessels

For human imaging, we used the system described by Rubinoff et al. [64]. We used Eq. 8 to estimate an NA of 0.05 in the retina, similar to the simulation and *ex vivo* measurements. All human imaging procedures were approved by Northwestern Institutional Review Board (IRB) and adhered to the Tenets of Helsinki. We illuminated the retina with 250 μW of power and acquired human retinal images consisting of 8192 A-lines × 16 B-scans repeated across a 3.8 mm field of view at a 25 kHz A-line rate.

3. Results

3.1. Contribution from multiple forward scattering in vis-OCT blood signal

We investigated how blood's scattering properties influence the detection of photons in vis-OCT. Fig. 3(A) plots a detected photon packet path from our MC simulation. The concentric rings plot the outer boundaries of each vessel layer. The photon packet launched from the origin followed the path of the green line. The green asterisk (*) highlights a scattering event, and a circled asterisk highlights a transmission or reflection across tissue regions. The photon packet in Fig. 3(A) was scattered 11 times inside the blood vessel. Notably, the photon packet travels mainly along the z-axis, consistent with a high scattering anisotropy (g = 0.987). This allows the photon packet to backscatter to nearly the same x-position as it launched, similar to the illustration in Fig. 1(D). Despite the multiple scattering events, we classified this photon packet to be Class I. Based on the optical properties shown in Table 1, the calculated MFP in blood is 8.5 μm; however, the photon packet travels 60 μm into the vessel (Fig. 3(A).

Table 1. Optical properties of tissues used in Monte Carlo simulation

	$\mu_s[cm^{-1}]$	$\mu_a[cm^{-1}]$	g [dimensionless]	Thickness [μm]
Retina	319	9	0.97	NA
Vessel Wall	284	4	0.84	4
Cell Free Zone	0.8	0.4	0.7	6
Blood	3415.5	176.1	0.984	68

Biomedical Optics EXPRESS

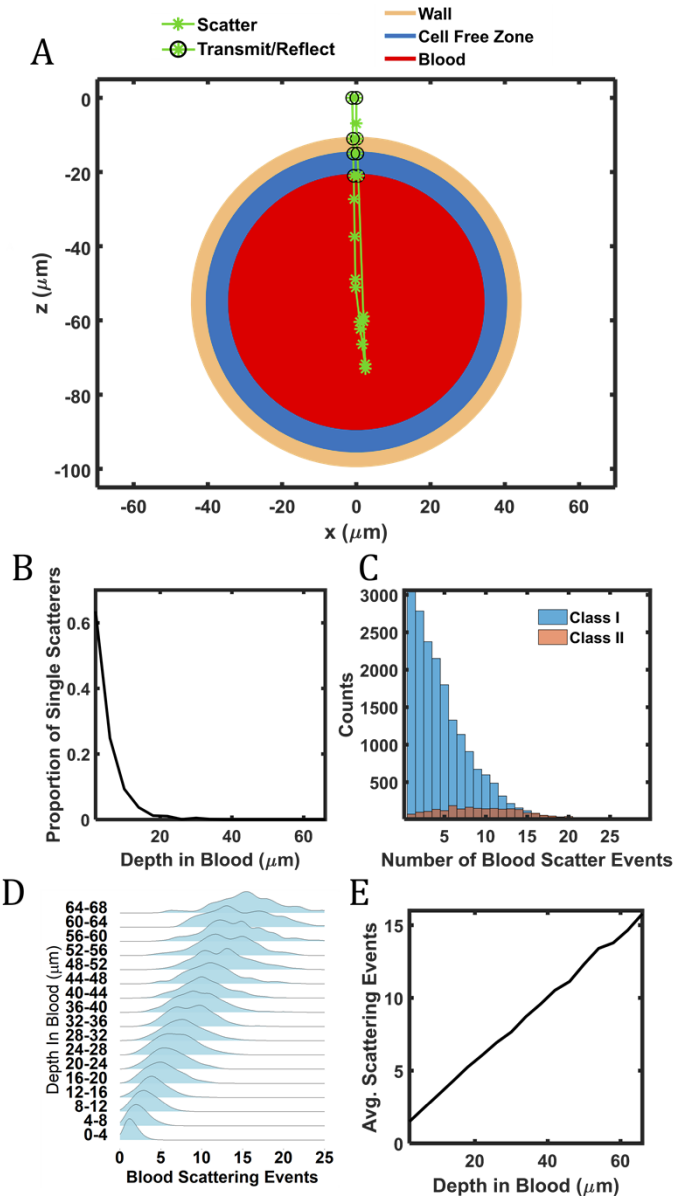

Fig. 3. (A) Simulated photon packet path (green line) and scattering events (green stars) in the blood vessel; (B) Proportions of detected singly-scattered photon packets; (C) Histogram showing the number of scattering events of the detected Class I and Class II photons; (D) Distributions of the number of scattering events at different depths in blood; (D) The average number of scattering events at different depths in blood.

Biomedical Optics EXPRESS

To assess whether the multiple scattering observed in Fig. 3(A) was a frequent occurrence, we measured the proportion of all detected singly scattered photons packets that entered the blood region (Fig. 3(B). Within the first 10 μm in blood, about 50% of photon packets are singly scattered, which is consistent with the predicted MFP near 8.5 μm. The proportion drops rapidly, where almost no detected photons are singly scattered after 17 μm into the blood region (2 MFPs). Considering that measurements deeper than 8.5 μm are necessary to provide sufficient attenuation contrast, it is reasonable to assume that retinal oximetry measurements are dominated by multiply scattered photons (excluding capillaries that may not generate multiple scattering due to low RBC counts).

Fig. 3(C) plots the detected Class I and Class II photons that entered the blood region. To improve the precision of the photon packet classification, we used $l_c = 1.4$ μm, the estimated vis-OCT full band resolution, rather than $l_c = 9$ μm, the STFT resolution. As shown in Fig. 3(C), Class I photons dominate. Figs. 3(B) & 3C collectively demonstrate that most detected photons are both Class I and multiply scattered photons. This observation is further emphasized by Fig. 3(D), which plots the fitted histograms of scattering events in blood from detected photons for different depths. The histograms are normalized with respect to their maximum values to show detail. The distributions show that, other than at the shallowest depths, photons are always multiple scattered. The average value of scattering events increases, and their distributions broaden as photon packets propagate deeper. Fig. 3(E) shows that the average value of scattering events is always > 1 and increases linearly with depth. Such a linear increase is consistent with the notion that a photon packet travels nearly along the same direction after each scattering event. The slope of this line corresponds to 1 blood scattering event for a photon step of 8.9 μm, consistent with the calculated MFP.

3.2. Measuring the SSF value

Fig. 4(A) plots the simulated A-line on a natural logarithm scale (referred to as 'log'). and illustrates the depth selection procedure for SSF measurement. From left to right, the first peak represents the anterior wall (AW) of the vessel, which is slightly convolved with the retinal tissue above it. Beneath the AW is a valley representing the cell-free zone (CFZ). The valley is smaller than expected from a completely 'scattering-free' region due to the limited 9-μm axial resolution. Beneath the CFZ is the blood maximum (BM), representing the start of blood signal decay (BSD) in the A-line. The distinct peak at the BM is collectively contributed by the finite MFP in blood, the size of the CFZ, and the limited 9-μm axial resolution. The depth location of BM in the A-line is about 10 μm deeper than the physical start of the vessel lumen and about 20 μm deeper than the AW peak. The blood signal decay (BSD) follows the BM and is consistent with log-scale decay described by the Beer-Lambert law [43]. When measuring the optical properties of blood *in vivo*, it is critical to start at least from the BM rather than assuming BSD occurs at the boundary of the AW and vessel lumen. Finally, the last peak represents the posterior wall (PW) of the vessel.

To measure the scattering coefficient, we modeled the BSD using a modified Eq. 5

$$\log(A(z)^2) = -2[\mu_{aHbO_2}(avg) + SSF \times \mu_{sHbO_2}(avg)]z \tag{11}$$

We include only the oxygenated coefficients since the simulated sO_2 was 100%. The term 'avg' indicates that simulation used optical properties that were the average value between 520 nm and 600 nm. . Although there are a handful of ways to extract $\mu_{sHbO_2}(avg)$ from this equation, we elected to compute a depth-average of Eq. 11, which we empirically found robust against noise [65]. The starting measurement depth is z_0 and the depth range is Δz. The full region of measurement is highlighted by the red dashed line. We first normalized $A(z)$ by its amplitude at

Biomedical Optics EXPRESS

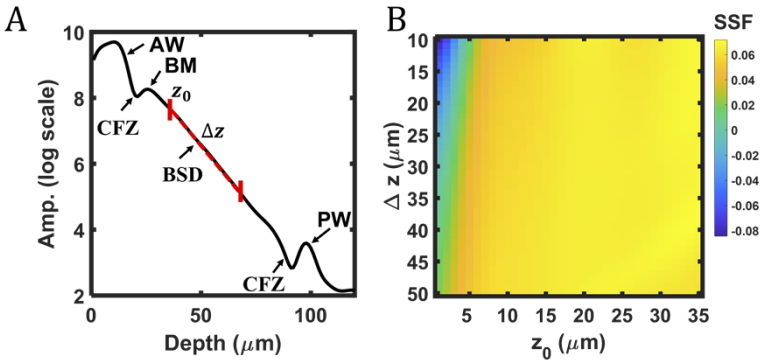

Fig. 4. (A) A simulated A-line at the center of the vessel, showing the anterior wall (AW), cell-free zone (CFZ), blood maximum (BM), blood signal decay (BSD), and posterior wall (PW); The red-dashed line highlights measurement depth range starting at z_0 and ranging Δz; (B) Measured SSF values from A-line in the panel A as a function of different z_0 and Δz.

z_0, which shifted the coordinate system to $z_0 = 0$. The average intensity becomes

$$\frac{1}{\Delta z}\int_0^{\Delta z} \log(A(z)^2)dz = -\frac{2}{\Delta z}[\mu_{aHbO_2}(avg) + SSF \times \mu_{sHbO_2}(avg)]\,\frac{\Delta z^2}{2} = [\mu_{aHbO_2}(avg) + SSF \times \mu_{sHbO_2}(avg)]\Delta z \tag{12}$$

Dividing by Δz, we are left only with the linear combination of $\mu_{aHbO_2}(avg)$ and $SSF \times \mu_{sHbO_2}(avg)$. By subtracting $\mu_{aHbO_2}(avg)$, whose value is from the literature, we are left with $SSF \times \mu_{sHbO_2}(avg)$, which can be compared with the literature μ_s value used in the simulation. The SSF can be calculated as

$$SSF = \frac{\frac{1}{\Delta z^2}\int_0^{\Delta z} \log(A(z)^2)dz - \mu_{aHbO_2}(avg)}{\mu_{sHbO_2}(avg)}. \tag{13}$$

Fig. 4(B) shows the SSF under various combinations of z_0 and Δz, where $z_0 = 0$ at the start of the vessel lumen. For z_0 between 0 µm and 5 µm, SSF ≤ 0, which is caused by choosing a depth before BM and is physically impossible. At z_0 = 10 µm, the approximate location of BM, SSF = 0.05-0.06, with slight variation for different Δz. For z_0 between 11 µm and 25 µm, SSF = 0.060-0.068. For $z_0 > 25$ µm, SSF is slightly greater than 0.07, which may be biased by the CFZ near the PW. Therefore, we selected $z_0 = 17$ µm and $\Delta z = 33$ µm, a range where the SSF = 0.064. The measured SSF is approximately 5-fold smaller than the literature packing factor $W = 0.3025$. Here, $\mu_{sHbO_2} = 0.064 \times \mu_{sHbO_2}(avg) = 222\ \mathrm{cm}^{-1}$, which is similar to the absorption coefficient $\mu_{aHbO_2}(avg) = 174\ \mathrm{cm}^{-1}$.

3.3. Influence of the number of scattering events on SSF

To understand how multiple scattering influences SSF, we set a graded threshold to the number of detected scattering events in blood. If a photon packet that entered the blood region is scattered more times than the set threshold, it was not included in the simulated A-line. Fig. 5(A) shows the simulated A-line for different scattering thresholds. The different shades of red plot different scattering threshold levels. The darkest shade has no threshold and collects photon packets from all scattering events (same as Fig. 4(A). A-line amplitude decays slower with higher threshold levels, consistent with the notion that increased multiple scattering reduces SSF. Specifically, when the threshold level is 1, the A-line is reconstructed by single-scattered Class I photon packets and decays within 20 µm in blood. As sO_2 calculation fits A-lines beyond 20 µm in blood, multiply scattered photons are required for accurate sO_2 measurement *in vivo*.

Biomedical Optics EXPRESS

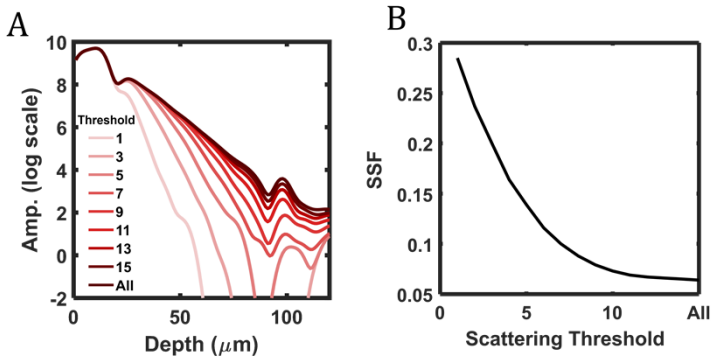

Fig. 5. (A) Simulated A-line at the center of the vessel after thresholding the number of detected scattering events in blood. Lighter shades indicate a lower threshold of detected scattering events; (B) The SSF value as a function of detected scattering threshold.

Additionally, it becomes clear that multiple scattering enables deeper photon penetration necessary for visualizing the PW. The PW becomes weak when the threshold level is less than 7 and invisible when the threshold level is less than 3. This suggests that multiple forward scattering also facilitates the visualization of the PW, a landmark commonly used in vis-OCT oximetry to indirectly measure μ_s [30]. Fig. 5(B) shows the relationship between SSF and the scattering threshold level, which decays approximately exponentially with the scattering threshold, asymptotically approaching 0.064 after threshold > 15. Thresholding 7 scattering events gives SSF = 0.116 and thresholding 2 scattering events gives SSF = 0.285, approaching the set $W = 0.3025$. We measured SSF = 0.424 when thresholding 1 scattering event; we did not include this data point due to insufficient signal-to-noise-ratio along the measured depths.

3.4. *Influence of numerical aperture on SSF*

As described in photon packet detection in our MC simulation, the detection NA acts as a spatial filter for photon scattering events. The detection aperture (radius) and angle limit an existing photon packet's position and propagation direction. Therefore, the detection criteria can potentially influence the measured SSF.

We examined the relationship between NA and SFF for $z_0 = 17$ μm and $\Delta z = 33$ μm based on the conclusion from the above section. The tested NA's are 0.015 to 0.112, which are based on physically reasonable imaging NA's in the human eye. In OCT, retinal imaging NA is almost always less than the maximum possible NA (e.g. 0.2 [57]), since researchers must consider limiting factors like reduced depth-of-focus, aberrations, and eye dilation [42]. Therefore, we varied the acceptance radius from 1.9 µm to 11.9 µm and varied the acceptance angle from 0.9° to 5.4°. We found that SSF varied between 0.02 to 0.09 (Fig. 6(A).

Fig. 6(B) plots the SSF values for physically possible NA values, which are along the diagonal of the matrix plotted in Fig. 6(A), and shows that SSF increases with increased NA. However, the relationship between NA and SSF is asymptotic near an NA of 0.08 (we extended the simulation to a maximum NA of 0.11 to validate the asymptote). For all the tested NA values, SSF is always less than 0.1, which is still less than one third of the literature value $W = 0.3025$. Fig. 6(C) plots the simulated A-line under different NA values. As NA increases, the amplitudes corresponding to AW and BM increase with respect to PW, which increases the slope of the blood decay and leads to an increased SSF. Conceptually, photons backscattered at shallower tissue depths do not travel far from the detection radius, making their detection more sensitive to acceptance angle rather than acceptance radius. Since the tissue exit angle of photons is depth-independent and stochastic, increased acceptance angles will result in increased numbers of detected photons from

Biomedical Optics EXPRESS

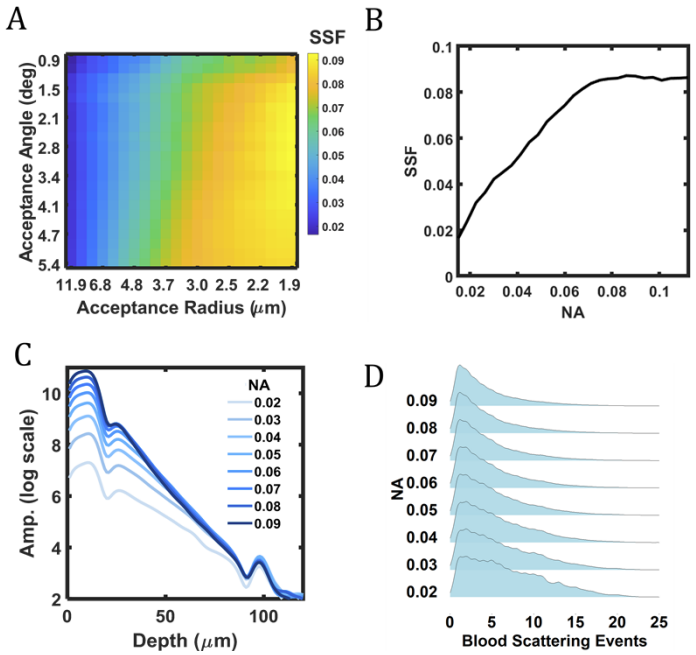

Fig. 6. (A) The SSF values as a function of optical detection radius and angle; (B) SSF as a function of numerical aperture (NA), which is the diagonal of the matrix in the panel A; (C) Simulated A-line at center of vessel for different NAs; lighter shades indicate lower NA; (D) Normalized distributions of scattering events in blood for different NAs.

shallower depths (depths near 25 μm in Fig. 6(C). Meanwhile, photons backscattered from deeper depths can travel farther from the detection radius and are filtered by both acceptance angle and radius. Unlike shallower-traveling photons, deeper-traveling photons experience the inverse relationship between acceptance radius and acceptance angle when varying NA. Therefore, the total number of photons detected from deeper depths vary less with changing NA (depths near 75 μm in Fig. 6(C). Hence, the relative difference between the number of accepted photons at shallower and deeper depths explains the observed change in SSF, despite no change in the optical properties of blood. Eventually, the SSF will plateau at higher NA's, when the acceptance radius becomes small enough, such that photons propagating at all depths are primarily filtered by acceptance radius.

Fig. 6(D) plots the fitted histograms of scattering events in blood from detected photon packets for different NA values, where each histogram is normalized by its respective maximum value. Fig. 6(D) confirms our previous hypothesis of increased detection of multiply scattered photon packets in Figs. 6(A)–6(C), where the histogram broadens with reduced NA values. Since the optical properties of blood remain unchanged, this difference is contributed by the changing detection criteria associated with NA.

It is important to note that this simulation presents a simplified view of the influence of OCT detection on SSF. Other variables, including the Gaussian beam profile, longitudinal chromatic aberrations, lateral chromatic aberrations, defocusing, eye geometry, oblique incidence, etc., will collectively influence the illumination and detection criteria as well [66]. However, the above simulation on the relationship between acceptance aperture and angle and SSF establishes a critical foundation for multiple scattering analysis in OCT. Such a relationship suggests no 'one-size-fits-all' SSF value exists.

Biomedical Optics EXPRESS

3.5. Ex vivo experimental results

Fig. 7 plots experimental vis-OCT measurements of *ex vivo* blood phantoms. All A-line reconstruction included correction for roll-off and background biases as previously reported [65,67]. Fig. 7(A) shows a representative B-scan image of the phantom with fully oxygenated ($sO_2 = 100\%$) blood at a hematocrit of 45%, the same as our simulation. The yellow dashed line highlights the location of the A-line plotted in Fig. 7(B). The A-line is an average of STFT A-lines from 528 nm – 588 nm (central band centered at 558 nm). In Fig. 7(B), there is a clear delineation between the AW (40 μm depth) and BM (57 μm depth), corresponding to the CFZ.

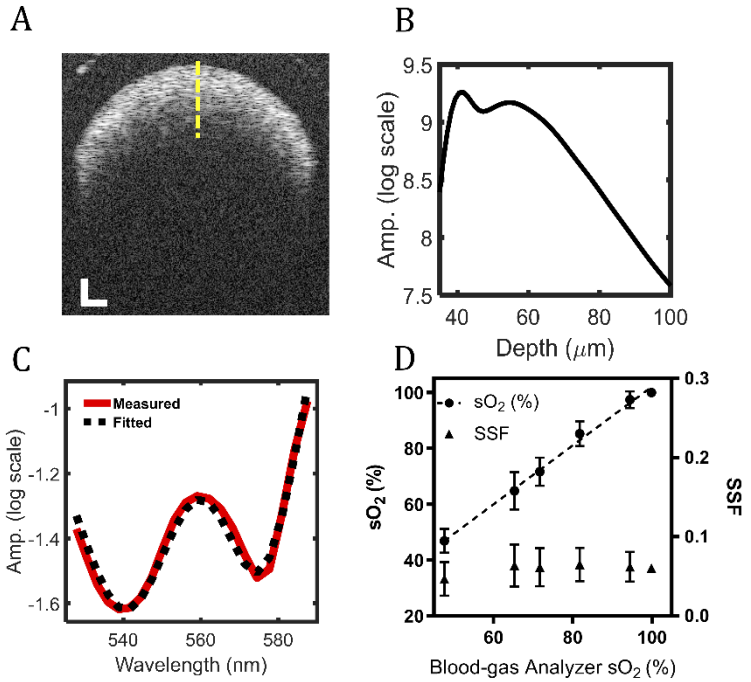

Fig. 7. (A) vis-OCT B-scan of fully oxygenated blood in a tube phantom; (B) A vis-OCT A-line at the center of tube phantom (yellow-dashed line) in the panel A; (C) Measured attenuation spectrum of fully oxygenated blood; (D) Measured sO_2 and SSF values at different pre-set oxygenation levels.

Fig. 7(C) plots a least-squares fit of the measured attenuation spectrum of fully oxygenated blood (red line) to its theoretical attenuation spectrum (black-dashed line). We performed least-squares fitting using Eq. 5 to measure sO_2 using the ratio of the oxygen-dependent coefficients [65] and estimate the SSF. The fitting ($R^2 = 0.98$) in Fig. 7(C) yields $sO_2 = 100\%$, $\mu_{sHbO_2}(avg) = 205\ cm^{-1}$, and SSF = 0.06, which agrees with the simulated SSF for fully oxygenated blood.

We measured sO_2 and SSF from five sO_2 levels between 40% and 100%. We bootstrapped 100 measurements for each level by shuffling each dataset and randomly selecting 50 B-scans. Fig. 7(D) shows the mean and SD of measured sO_2 (circles) and SSF (triangles). The black dashed line shows the linear best fit relationship ($y = 1.05x - 3.30$) between the blood-gas machine measurements and vis-OCT measurements, indicating excellent agreement between these two independent measurements. The average SSF is 0.060 +/- 0.021, and the average spectroscopic fit R^2 is 0.99. The agreement between simulated and experimentally measured SSF values suggests that our work does not contradict the previously suggested packing factor in whole blood [9] but, instead, adds an additional correction for vis-OCT oximetry.

Biomedical Optics EXPRESS

3.6. *In vivo experimental results*

We validated SSF measurement in vis-OCT imaging of human retinas. Fig. 8(A) shows a B-scan image from a 23-year-old male volunteer. We investigated one major vein and one major artery, as highlighted by 1 and 2, respectively. The yellow dashed lines highlight the locations of A-lines plotted in Figs. 8(B) & 8C. The A-lines are an average of STFT A-lines from 528 nm – 588 nm. The vein plotted in Fig. 8(B) clearly delineated the AW and BM, similar to the simulated A-line (Fig. 4(A) and ex vivo A-line (Fig. 7(B). In the artery plotted in Fig. 8(C), this delineation is less obvious, and there is a change in slope near 260 μm depth where the BM is typically located, which can be caused by higher, pulsatile blood flow in arteries leading to less precise spatial averaging. We also observe a small valley near the center of the vessel in Fig. 8(C), which may also be associated with more turbulent flow patterns in arteries.

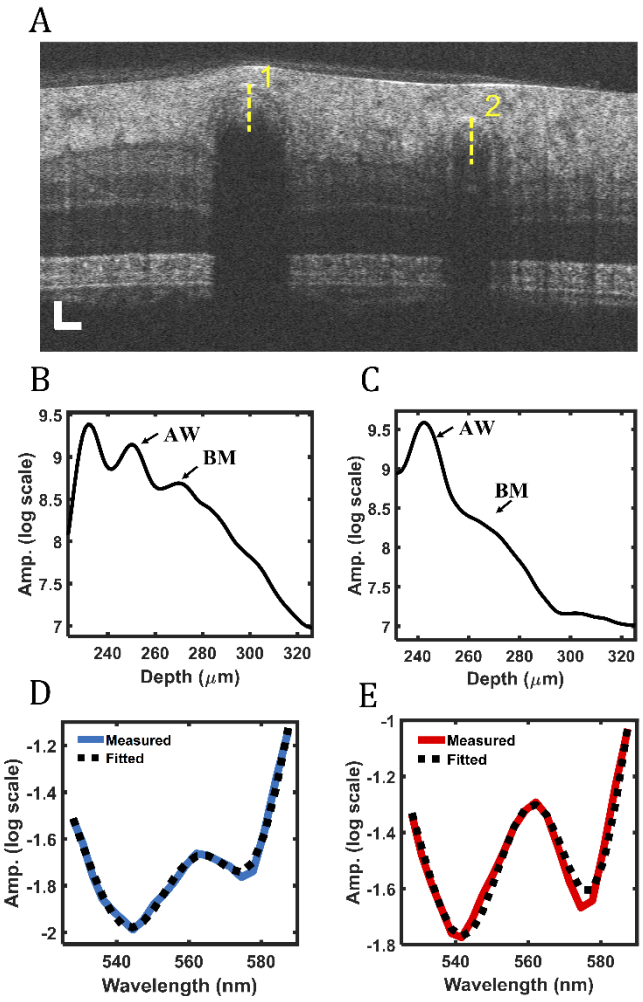

Fig. 8. (A) Vis-OCT B-scan image of a human retina, where a vein is labeled by 1 and an artery is labeled by 2; (B) Vis-OCT A-line of the vein from the highlighted position in the panel A; (C) Vis-OCT A-line of the artery from the highlighted position in the panel (A); (D) Measured attenuation spectrum from the highlighted vein in the panel A; (E) Measured attenuation spectrum from the highlighted artery in the panel A.

Biomedical Optics EXPRESS

We calculated sO_2 and SSF by fitting the wavelength-dependent attenuation spectrum with the theoretical spectrum [65]. The measured SSF agreed with our simulated and e*x vivo* experimental results. Fig. 8(D) shows a least-squares fit of the attenuation spectrum measured in the vein. The best fit yields $sO_2 = 59\%$ ($R^2 = 0.99$) and SSF = 0.07. Fig. 8(E) shows the fitting results for the artery, where $sO_2 = 100\%$ ($R^2 = 0.97$) and SSF = 0.07.

4. Discussion and conclusion

Accurate vis-OCT oximetry remains challenging because of systemic uncertainties introduced by multiple scattering. This work establishes a new correction factor SSF to account for multiply forward scattered photons in blood. Using MC simulation, we found that SSF is near 0.06, significantly smaller than the reported packing factor ($W = 0.3025$) [9,30,54]. Documented photon packets' trajectories indicate that most detected photon packets belong to Class I, meaning they are ballistic photon packets and return to the detector with a small deviation from their incident axis. We found that these Class I photon packets were scattered multiple times, which is only possible if they are primarily forward scattered. We further investigated how different NAs influence the measured SSF. We found that physically reasonable NA values in the human retinal imaging yield SSF values between 0.02 and 0.09, suggesting that NA substantially impacts the measured SSF. As a result, vis-OCT should not use rigid, *a priori* models for retinal oximetry, especially with different hardware designs and imaging of different eyes.

We imaged *ex vivo* bovine blood phantoms using vis-OCT as the first validation of our simulation findings. After correcting systemic biases from the background and roll-off, we measured sO_2 and SSF and compared vis-OCT measurements with blood-oxygen analyzer measurements. We found that the average SSF was 0.060 +/- 0.021, almost identical to the simulated results. We further performed vis-OCT sO_2 measurements in the human retina and found that SSF was 0.06 and measured sO_2 values consistent with physiological ranges for arteries and veins. This work is the first comprehensive investigation and validation of blood's attenuation spectrum in vis-OCT using simulation, *ex vivo* phantom and human retinal imaging.

Using the packing factor to scale the scattering coefficient in our MC simulation resulted in SSF values in excellent agreement with experimental data. As suggested in the literature, the packing factor is the result of correlated scatterings among densely packed RBCs [9,28,68,69]. As RBC concentration increases, coherent interferences can affect the far-field scattered field, which is nonlinearly correlated with RBC density and is likely dependent on the orientations of individual RBCs. While MC simulation does not directly account for orientation-dependent scattering, it can replicate their statistical influence by scaling the input μ_s by W. Furthermore, previous experimental tests of blood's scattering coefficient were performed using an integration sphere [10,11,28,46,70], which does not spatially filter detected photons as vis-OCT does. Our SSF combines the influence of scattering effects from blood hemodynamics (e.g., packing factor) and spatial filtering by the imaging modality (e.g., acceptance aperture and angle) on the effective μ_s measured by vis-OCT.

One limitation in our simulation is the assumption of blood as a homogenous medium. In reality, RBC packing density and orientations are affected by blood flow, blood velocity, vessel size, and incident angle [11,49,71–73]. These factors can alter scattering cross-section and directionality, changing the optical properties assumed in this work. Although significant spatial averaging may suppress these variations, researchers should carefully monitor the variability of SSF to ensure a suitable oximetry model. Additionally, factors outside of light-tissue interaction such as the confocal function and roll-off may impact the measured attenuation, particularly if they are spectrally dependent. Since we are using relatively low NAs in this study, the depth of focus (Rayleigh length = 71 μm at NA = 0.05) is sufficiently long to have a negligible influence on the results. In addition, in clinical imaging, the focal plane of the human retina is not known *a priori*, and strong motions and chromatic aberrations make its correction nontrivial.

Biomedical Optics EXPRESS

We investigated a suite of parameters influencing vis-OCT detection and concluded that a combination of low NA and multiple forward scattering causes a significant reduction of the measured scattering coefficient of blood. This enables the detection of ballistic photons penetrating deep into retinal vessels and absorption-dominated spectroscopic measurements. In the future, researchers should use these conclusions to inform parameters in sO_2 models.

Funding. National Institutes of Health (R01EY019949, R01EY026078, R01EY029121, T32GM142604, U01EY033001).

Disclosures. R. Fang, None; I. Rubinoff, None; H F. Zhang, Opticent Inc, which did not support this work

Data Availability. Data underlying the results presented in this paper are not yet publicly available but may be obtained from the authors upon request.

References

1. J. M. Schmitt, "Optical coherence tomography (OCT): a review," IEEE J. Sel. Top. Quantum Electron. **5**(4), 1205–1215 (1999).
2. D. Huang, E. A. Swanson, C. P. Lin, J. S. Schuman, W. G. Stinson, W. Chang, M. R. Hee, T. Flotte, K. Gregory, C. A. Puliafito, and J. G. Fujimoto, "Optical coherence tomography," Science **254**(5035), 1178–1181 (1991).
3. M. Wojtkowski, "High-speed optical coherence tomography: basics and applications," Appl. Opt. **49**(16), D30–D61 (2010).
4. J. G. Fujimoto, W. Drexler, J. S. Schuman, and C. K. Hitzenberger, "Optical coherence tomography (OCT) in ophthalmology: introduction," Opt. Express **17**(5), 3978–3979 (2009).
5. M. Almasian, N. Bosschaart, T. G. van Leeuwen, and D. J. Faber, "Validation of quantitative attenuation and backscattering coefficient measurements by optical coherence tomography in the concentration-dependent and multiple scattering regime," J. Biomed. Opt **20**(12), 121314 (2015).
6. P. Gong, M. Almasian, G. Van Soest, D. M. De Bruin, T. G. Van Leeuwen, D. D. Sampson, and D. J. Faber, "Parametric imaging of attenuation by optical coherence tomography: review of models, methods, and clinical translation," J. Biomed. Opt. **25**(04), 1 (2020).
7. S. Liu, Y. Sotomi, J. Eggermont, G. Nakazawa, S. Torii, T. Ijichi, Y. Onuma, P. W. Serruys, B. P. Lelieveldt, and J. Dijkstra, "Tissue characterization with depth-resolved attenuation coefficient and backscatter term in intravascular optical coherence tomography images," J. Biomed. Opt **22**(09), 1 (2017).
8. D. J. Smithies, T. Lindmo, Z. Chen, J. S. Nelson, and T. E. Milner, "Signal attenuation and localization in optical coherence tomography studied by Monte Carlo simulation," Phys. Med. Biol. **43**(10), 3025–3044 (1998).
9. N. Bosschaart, G. J. Edelman, M. C. Aalders, T. G. van Leeuwen, and D. J. Faber, "A literature review and novel theoretical approach on the optical properties of whole blood," Lasers Med. Sci. **29**(2), 453–479 (2014).
10. M. Friebel, J. Helfmann, U. J. Netz, and M. C. Meinke, "Influence of oxygen saturation on the optical scattering properties of human red blood cells in the spectral range 250 to 2000nm," J. Biomed. Opt. **14**(3), 034001 (2009).
11. A. Roggan, M. Friebel, K. Dörschel, A. Hahn, and G. J. Mueller, "Optical properties of circulating human blood in the wavelength range 400-2500 nm," J. Biomed. Opt. **4**(1), 36–46 (1999).
12. D. J. Faber, M. C. G. Aalders, E. G. Mik, B. A. Hooper, M. J. C. van Gemert, and T. G. van Leeuwen, "Oxygen saturation-dependent absorption and scattering of blood," Phys. Rev. Lett. **93**(2), 028102 (2004).
13. F. E. Robles, C. Wilson, G. Grant, and A. Wax, "Molecular imaging true-colour spectroscopic optical coherence tomography," Nat. Photonics **5**(12), 744–747 (2011).
14. X. Shu, L. Beckmann, and H. F. Zhang, "Visible-light optical coherence tomography: a review," J. Biomed. Opt. **22**(12), 121707 (2017).
15. C. Veenstra, S. Kruitwagen, D. Groener, W. Petersen, W. Steenbergen, and N. Bosschaart, "Quantification of total haemoglobin concentrations in human whole blood by spectroscopic visible-light optical coherence tomography," Sci. Rep. **9**(1), 15115 (2019).
16. C. W. Lu, C. K. Lee, M. T. Tsai, Y. M. Wang, and C. C. Yang, "Measurement of the hemoglobin oxygen saturation level with spectroscopic spectral-domain optical coherence tomography," Opt. Lett. **33**(5), 416–418 (2008).
17. A. L. Oldenburg, C. Y. Xu, and S. A. Boppart, "Spectroscopic optical coherence tomography and microscopy," IEEE J. Select. Topics Quantum Electron. **13**(6), 1629–1640 (2007).
18. R. A. Linsenmeier and H. F. Zhang, "Retinal oxygen: from animals to humans," Prog. Retinal Eye Res. **58**, 115–151 (2017).
19. W. Z. Liu, S. J. Wang, B. Soetikno, J. Yi, K. V. Zhang, S. Y. Chen, R. A. Linsenmeier, C. M. Sorenson, N. Sheibani, and H. F. Zhang, "Increased retinal oxygen metabolism precedes microvascular alterations in type 1 diabetic mice," Invest. Ophthalmol. Visual Sci. **58**(2), 981 (2017).
20. S. Y. Chen, J. Yi, W. Z. Liu, V. Backman, and H. F. Zhang, "Monte Carlo Investigation of Optical Coherence Tomography Retinal Oximetry," IEEE Trans. Biomed. Eng. **62**(9), 2308–2315 (2015).
21. S. Chen, J. Yi, and H. F. Zhang, "Measuring oxygen saturation in retinal and choroidal circulations in rats using visible light optical coherence tomography angiography," Biomed. Opt. Express **6**(8), 2840–2853 (2015).

Biomedical Optics EXPRESS

22. J. Yi, W. Liu, S. Chen, V. Backman, N. Sheibani, C. M. Sorenson, A. A. Fawzi, R. A. Linsenmeier, and H. F. Zhang, "Visible light optical coherence tomography measures retinal oxygen metabolic response to systemic oxygenation," Light: Sci. Appl. **4**(9), e334 (2015).
23. S. Pi, A. Camino, X. Wei, J. Simonett, W. Cepurna, D. Huang, J. C. Morrison, and Y. Jia, "Rodent retinal circulation organization and oxygen metabolism revealed by visible-light optical coherence tomography," Biomed. Opt. Express **9**(11), 5851–5862 (2018).
24. S. Pi, A. Camino, W. Cepurna, X. Wei, M. Zhang, D. Huang, J. Morrison, and Y. Jia, "Automated spectroscopic retinal oximetry with visible-light optical coherence tomography," Biomed. Opt. Express **9**(5), 2056–2067 (2018).
25. S. Chen, X. Shu, P. L. Nesper, W. Liu, A. A. Fawzi, and H. F. Zhang, "Retinal oximetry in humans using visible-light optical coherence tomography," Biomed. Opt. Express **8**(3), 1415–1429 (2017).
26. S. Pi, T. T. Hormel, X. Wei, W. Cepurna, B. Wang, J. C. Morrison, and Y. Jia, "Retinal capillary oximetry with visible light optical coherence tomography," Proc. Natl. Acad. Sci. U.S.A. **117**(21), 11658–11666 (2020).
27. D. J. Faber, E. G. Mik, M. C. Aalders, and T. G. van Leeuwen, "Toward assessment of blood oxygen saturation by spectroscopic optical coherence tomography," Opt. Lett. **30**(9), 1015–1017 (2005).
28. M. Meinke, G. Müller, J. Helfmann, and M. Friebel, "Empirical model functions to calculate hematocrit-dependent optical properties of human blood," Appl. Opt. **46**(10), 1742–1753 (2007).
29. W. G. Zijlstra, A. Buursma, and O. W. van Assendelft, *Visible and Near Infrared Absorption Spectra of Human and Animal Haemoglobin: Determination and Application* (VSP, 2000).
30. J. Yi, Q. Wei, W. Liu, V. Backman, and H. F. Zhang, "Visible-light optical coherence tomography for retinal oximetry," Opt. Lett. **38**(11), 1796–1798 (2013).
31. W. Song, W. Shao, W. Yi, R. Liu, M. Desai, S. Ness, and J. Yi, "Visible light optical coherence tomography angiography (vis-OCTA) facilitates local microvascular oximetry in the human retina," Biomed. Opt. Express **11**(7), 4037–4051 (2020).
32. S. P. Chong, C. W. Merkle, C. Leahy, H. Radhakrishnan, and V. J. Srinivasan, "Quantitative microvascular hemoglobin mapping using visible light spectroscopic optical coherence tomography," Biomed. Opt. Express **6**(4), 1429–1450 (2015).
33. S. P. Chong, C. W. Merkle, H. Radhakrishnan, C. Leahy, A. Dubra, Y. N. Sulai, and V. J. Srinivasan, "Optical coherence imaging of microvascular oxygenation and hemodynamics," in *CLEO: Applications and Technology*, (Optical Society of America, 2014), ATh1O. 2.
34. R. Liu, W. Song, V. Backman, and J. Yi, "Quantitative quality-control metrics for in vivo oximetry in small vessels by visible light optical coherence tomography angiography," Biomed. Opt. Express **10**(2), 465–486 (2019).
35. G. Yao and L. V. Wang, "Monte Carlo simulation of an optical coherence tomography signal in homogeneous turbid media," Phys. Med. Biol. **44**(9), 2307–2320 (1999).
36. I. Rubinoff, R. V. Kuranov, and H. F. Zhang, "Intrinsic spectrally-dependent background in spectroscopic visible-light optical coherence tomography," Biomed. Opt. Express **12**(1), 110–124 (2021).
37. E. Yuan, P. Si, Y. Winetraub, S. Shevidi, and A. de la Zerda, "A spectral demixing model for triplex in vivo imaging of optical coherence tomography contrast agents," Acs Photonics **7**(4), 893–900 (2020).
38. L. Wang, S. L. Jacques, and L. Zheng, "MCML—Monte Carlo modeling of light transport in multi-layered tissues," Comput. Methods Programs in Biomed. **47**(2), 131–146 (1995).
39. B. G. Yust, L. C. Mimun, and D. K. Sardar, "Optical absorption and scattering of bovine cornea, lens, and retina in the near-infrared region," Lasers Med. Sci. **27**(2), 413–422 (2012).
40. S. Aumann, S. Donner, J. Fischer, and F. Müller, "Optical coherence tomography (OCT): principle and technical realization," *High Resolution Imaging in Microscopy and Ophthalmol.* 59–85 (2019).
41. S. Farsiu, J. Christofferson, B. Eriksson, P. Milanfar, B. Friedlander, A. Shakouri, and R. Nowak, "Statistical detection and imaging of objects hidden in turbid media using ballistic photons," Appl. Opt. **46**(23), 5805–5822 (2007).
42. F. L. Pedrotti, L. M. Pedrotti, and L. S. Pedrotti, *Introduction to optics* (Cambridge University Press, 2017).
43. D. F. Swinehart, "The beer-lambert law," J. Chem. Educ. **39**(7), 333 (1962).
44. L. Thrane, H. T. Yura, and P. E. Andersen, "Analysis of optical coherence tomography systems based on the extended Huygens–Fresnel principle," J. Opt. Soc. Am. A **17**(3), 484–490 (2000).
45. L. Durak and O. Arikan, "Short-time Fourier transform: two fundamental properties and an optimal implementation," IEEE Trans. Signal Process. **51**(5), 1231–1242 (2003).
46. M. Friebel, A. Roggan, G. J. Müller, and M. C. Meinke, "Determination of optical properties of human blood in the spectral range 250 to 1100 nm using Monte Carlo simulations with hematocrit-dependent effective scattering phase functions," J. Biomed. Opt. **11**(3), 034021 (2006).
47. H. Nilsson and G. E. Nilsson, "Monte Carlo simulations of light interaction with blood vessels in human skin in the red-wavelength region," in *Optical Diagnostics of Biological Fluids III*, (International Society for Optics and Photonics, 1998), 44–53.
48. M. Hammer, A. Roggan, D. Schweitzer, and G. Muller, "Optical properties of ocular fundus tissues-an in vitro study using the double-integrating-sphere technique and inverse Monte Carlo simulation," Phys. Med. Biol. **40**(6), 963–978 (1995).
49. D. Sakota and S. Takatani, "Quantitative analysis of optical properties of flowing blood using a photon-cell interactive Monte Carlo code: effects of red blood cells' orientation on light scattering," J. Biomed. Opt. **17**(5), 057007 (2012).

Biomedical Optics EXPRESS

50. M. Kirillin, I. Meglinski, V. Kuzmin, E. Sergeeva, and R. Myllylä, "Simulation of optical coherence tomography images by Monte Carlo modeling based on polarization vector approach," Opt. Express **18**(21), 21714–21724 (2010).
51. H. L. Goldsmith, G. R. Cokelet, and P. Gaehtgens, "Robin Fahraeus: evolution of his concepts in cardiovascular physiology," Am. J. Physiol.-Heart and Circulatory Physiol. **257**(3), H1005–H1015 (1989).
52. J. Lauri, A. Bykov, and T. Fabritius, "Quantification of cell-free layer thickness and cell distribution of blood by optical coherence tomography," J. Biomed. Opt. **21**(4), 040501 (2016).
53. M. C. Meinke, G. J. Müller, J. Helfmann, and M. Friebel, "Optical properties of platelets and blood plasma and their influence on the optical behavior of whole blood in the visible to near infrared wavelength range," J. Biomed. Opt. **12**(1), 014024 (2007).
54. H. H. Billett, "Hemoglobin and hematocrit," *Clinical Methods: The History, Physical, and Laboratory Examinations*, 3rd edition (Butterworth, 1990).
55. D. Toublanc, "Henyey–Greenstein and Mie phase functions in Monte Carlo radiative transfer computations," Appl. Opt. **35**(18), 3270–3274 (1996).
56. J. Skaar, "Fresnel equations and the refractive index of active media," Phys. Rev. E **73**(2), 026605 (2006).
57. D. A. Atchison, G. Smith, and G. Smith, *Optics of the Human Eye* (Butterworth-Heinemann Oxford, 2000), Vol. 2.
58. D. Van Norren and L. Tiemeijer, "Spectral reflectance of the human eye," Vision Res. **26**(2), 313–320 (1986).
59. J. A. Izatt and M. A. Choma, "Theory of Optical Coherence Tomography," in *Optical Coherence Tomography: Technology and Applications*, W. Drexler and J. G. Fujimoto, eds. (Springer Berlin Heidelberg, 2008), pp. 47–72.
60. X. Zhang, L. Beckmann, D. A. Miller, G. Shao, Z. Cai, C. Sun, N. Sheibani, X. Liu, J. Schuman, and M. Johnson, "In vivo imaging of Schlemm's canal and limbal vascular network in mouse using visible-light OCT," Invest. Ophthalmol. Visual Sci. **61**(2), 23 (2020).
61. ThorLabs, "400 to 700 nm Wavelength Range," (2022), retrieved https://www.thorlabs.com/newgrouppage9.cfm?objectgroup_id=2910&pn=LSM03-VIS#.
62. R. V. Kuranov, J. Qiu, A. B. McElroy, A. Estrada, A. Salvaggio, J. Kiel, A. K. Dunn, T. Q. Duong, and T. E. Milner, "Depth-resolved blood oxygen saturation measurement by dual-wavelength photothermal (DWP) optical coherence tomography," Biomed. Opt. Express **2**(3), 491 (2011).
63. G. R. Kelman, "Digital computer procedure for the conversion of PCO2, into blood CO2 content," Respir. Physiol. **3**(1), 111–115 (1967).
64. I. Rubinoff, R. V. Kuranov, Z. Ghassabi, Y. Wang, L. Beckmann, D. A. Miller, B. Tayebi, G. Wollstein, H. Ishikawa, J. S. Schuman, and H. F. Zhang, "Adaptive spectroscopic visible-light optical coherence tomography for human retinal oximetry," bioRxiv (2021).
65. R. V. K. Ian Rubinoff, Zeinab Ghassabi, Yuanbo Wang, Lisa Beckmann, David A. Miller, Behnam Tayebi, Gadi Wollstein, Hiroshi Ishikawa, Joel S. Schuman, and Hao F. Zhang, "Adaptive spectroscopic visible-light optical coherence tomography for human retinal oximetry," bioRxiv (2021).
66. Y. Pan, E. Lankenou, J. Welzel, R. Birngruber, and R. Engelhardt, "Optical coherence-gated imaging of biological tissues," IEEE J. Sel. Top. Quantum Electron. **2**(4), 1029–1034 (1996).
67. I. Rubinoff, B. Soetikno, D. A. Miller, I. Rischall, A. Fawzi, R. Kuranov, and H. F. Zhang, "Spectrally dependent roll-off in visible-light optical coherence tomography," Opt. Lett. **45**(9), 2680–2683 (2020).
68. V. Twersky, "Absorption and multiple scattering by biological suspensions," J. Opt. Soc. Am. **60**(8), 1084–1093 (1970).
69. A. Ishiniaru and Y. Kuga, "Attenuation constant of a coherent field in a dense distribution of particles," J. Opt. Soc. Am. **72**(10), 1317–1320 (1982).
70. A. N. Yaroslavsky, I. V. Yaroslavsky, T. Goldbach, and H.-J. Schwarzmaier, "Optical properties of blood in the near-infrared spectral range," in *Optical Diagnostics of Living Cells and Biofluids*, (International Society for Optics and Photonics, 1996), 314–324.
71. M. Friebel, J. Helfmann, G. J. Müller, and M. C. Meinke, "Influence of shear rate on the optical properties of human blood in the spectral range 250 to 1100 nm," J. Biomed. Opt. **12**(5), 054005 (2007).
72. W. Steenbergen, R. Kolkman, and F. de Mul, "Light-scattering properties of undiluted human blood subjected to simple shear," J. Opt. Soc. Am. A **16**(12), 2959–2967 (1999).
73. A. M. Enejder, J. Swartling, P. Aruna, and S. Andersson-Engels, "Influence of cell shape and aggregate formation on the optical properties of flowing whole blood," Appl. Opt. **42**(7), 1384–1394 (2003).